

Centralized Information Interaction for Salient Object Detection

Jiang-Jiang Liu* Zhi-Ang Liu* Ming-Ming Cheng[†]
 CS, Nankai University

Abstract

The U-shape structure has shown its advantage in salient object detection for efficiently combining multi-scale features. However, most existing U-shape based methods focused on improving the bottom-up and top-down pathways while ignoring the connections between them. This paper shows that by centralizing these connections, we can achieve the cross-scale information interaction among them, hence obtaining semantically stronger and positionally more precise features. To inspire the potential of the newly proposed strategy, we further design a relative global calibration module that can simultaneously process multi-scale inputs without spatial interpolation. Benefiting from the above strategy and module, our proposed approach can aggregate features more effectively while introducing only a few additional parameters. Our approach can cooperate with various existing U-shape-based salient object detection methods by substituting the connections between the bottom-up and top-down pathways. Experimental results demonstrate that our proposed approach performs favorably against the previous state-of-the-arts on five widely used benchmarks with less computational complexity. The source code will be publicly available.

1. Introduction

As a fundamental component of low-level computer vision and benefiting from its category-agnostic character, salient object detection has been widely applied in various downstream vision tasks, such as weakly supervised semantic segmentation [16, 56], visual tracking [14], content-aware image editing [6], and robot navigation [7]. Traditional salient object detection methods depend heavily on hand-crafted feature detectors. These detectors cannot utilize the rich high-level semantic information hidden in the image and dataset, making them fail in complex scenes. With the popularization of commercial GPUs, convolutional neural networks (CNNs) based methods have been developing rapidly in recent years for their capability of ex-

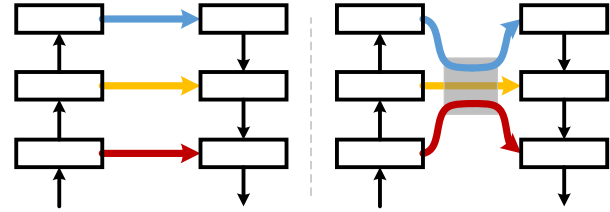


Figure 1. Conceptual diagram of our proposed centralized information interaction strategy. **Left:** Typical U-shape structure which connects the corresponding stages in the bottom-up and top-down pathways directly; **Right:** Our proposed centralized strategy. The rounded gray rectangle refers to a shared module that can parallelly process all stages (scales) of features in a stage-wise manner.

tracting both high-level semantics and low-level textures of multiple scales.

One representative architecture for salient object detection is the U-shape structure [27, 44]. As illustrated in the left part of Fig. 1, a typical U-shape structure consists of a bottom-up pathway, a top-down pathway, and several connections between them. Among the methods that aim to advance the U-shape structures, most of them either focus on improving the bottom-up pathway’s feature extraction capability or enhancing the top-down pathway’s feature aggregation ability or both of them. However, the connections between the bottom-up and top-down pathways are neglected. The usual practice is to directly connect the corresponding stages. In this paper, different from the methods mentioned above, we investigate how to augment the representation capability of the extracted features by redesigning the connections between the bottom-up and top-down pathways rather than the pathways themselves.

A straightforward way to achieve the purpose mentioned above is to fuse the extracted multi-scale features directly [26, 39]. However, an inevitable step of cross-scale features fusing is spatial interpolation. As demonstrated in Fig. 2, the intermediate feature map being down-sampled first and then up-sampled differs greatly from its original values, and vice versa. This phenomenon worsens when the down-sampling rate increases, as more spatial location information is missed.

To this end, we propose to encode the cross-scale information into the filters instead of the features, where no spa-

*Indicates equal contributions.

[†]Indicates corresponding author.

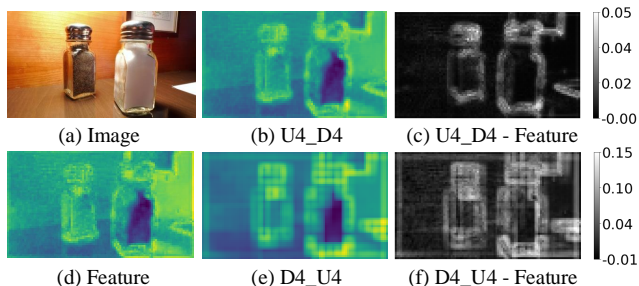


Figure 2. An example case showing the impact of spatial interpolation. (a) is the source image and (d) is the corresponding output feature map of ResNet-18’s *res1* stage. (b) is obtained by directly $4\times$ bilinear up-sampling and then $4\times$ bilinear down-sampling on (d), while (e) is down-sampled first and then up-sampled. (c,f) are the difference maps of (b,d) and (e,d), respectively. It can be seen that even the simplest spatial interpolation operations can cause obvious differences.

tial interpolation is required. As shown in the right part of Fig. 1, the multi-scale features extracted from the bottom-up pathway are parallelly processed by a centralized module whose parameters are shared across scales before being used to build the top-down pathway. We call the proposed filter-level information interaction strategy, centralized information interaction (CII). CII faithfully preserves the exact spatial locations within each input scale, meanwhile achieves cross-scale information interaction and fundamentally avoids the negative effects caused by spatial interpolation of features. To cooperate with the new normal that the inputs of the shared module in CII are naturally of multiple scales, we further propose a relative global calibration module (RGC). By exploring the global information related to each scale of feature, RGC achieves a balance between essential global semantic and local details. We also show that with a slight modification on the input flow of the RGC module, the overall performance can be further promoted nearly for free.

To evaluate the performance of the proposed approach, we report results on five popular salient object detection benchmarks. We conduct extensive ablation studies and show numerous visual examples to help readers better understand the impacts of different components of the proposed approach. Our approach only introduces $\sim 4\%$ additional parameters regarding the backbone network. It can be trained end-to-end on a single RTX-2080Ti GPU within 1.5 hours on a set of 10,553 images. To sum up, our main contributions can be summarized as follows:

- We design a centralized information interaction strategy to efficiently resolve the contradiction between cross-scale information interaction and spatial location information preservation.
- We propose a relative global calibration module that

can effectively exploit the relative global information related to each different spatial scale and obtain substantial improvements.

2. Related Work

In this section, we briefly review the recent representative work on salient object detection, multi-scale feature aggregation, and multi-scale and attention modules.

2.1. Salient Object Detection

Early salient object detection methods were usually based on intrinsic cues and hand-crafted features [5, 19, 24, 41]. More details can be found in recent surveys [1, 2, 50, 52]. Among the deep-learning-based methods, many adopted the idea of recurrent refinement [49, 51] to refine the predictions iteratively. Some methods treated this problem stage-wisely [32, 48, 59] by decoupling it into multiple stages. To get predictions with more precise boundaries, [43, 54, 75] designed new loss functions while [9, 55, 72, 75] introduced extra supervisions. [9, 21, 33, 53, 70, 73] proposed various types of attention mechanisms and achieved substantial improvements. Among the above methods, a majority of them were based on the classic U-shape structure. [45, 67, 68, 73, 74] attached additional multi-scale modules after the bottom-up pathway to generate more powerful features, while [15, 30, 37, 40, 69] combined the extracted multi-scale features in different ways within the top-down pathway to generate richer features.

2.2. Multi-scale Features Aggregation

As a pioneer, FCNs [36] directly aggregated the features from low-level stages with the ones from the most high-level stage for more precise semantic segmentation. Similarly, U-Net [44] and FPNs [27] further incorporated a top-down pathway to sequentially combine the extracted multi-scale features from high- to low-levels. As followers, PANet [35] adopted another bottom-up pathway on top of FPN while ASFF [34] proposed to fuse more stages of features in the top-down pathway of FPN. EfficientDet [46] proposed a BiFPN layer and repeated it multiple times. RFP [42] proposed to repeatedly pass the features through the bottom-up backbone to enrich the representation power of FPN. Recently, NAS-FPN [12] and Auto-FPN [61] applied the neural architecture search [76] to discover the optimal FPN structure in a data-driven manner automatically.

2.3. Multi-scale and Attention Modules

Deeplabv2 [3] proposed an atrous spatial pyramid pooling (ASPP) module to capture contextual information using different dilation convolutions. DenseASPP [65] improved ASPP with dense connections. PSPNet [71] utilized a pyramid pooling module (PPM) to aggregate contextual

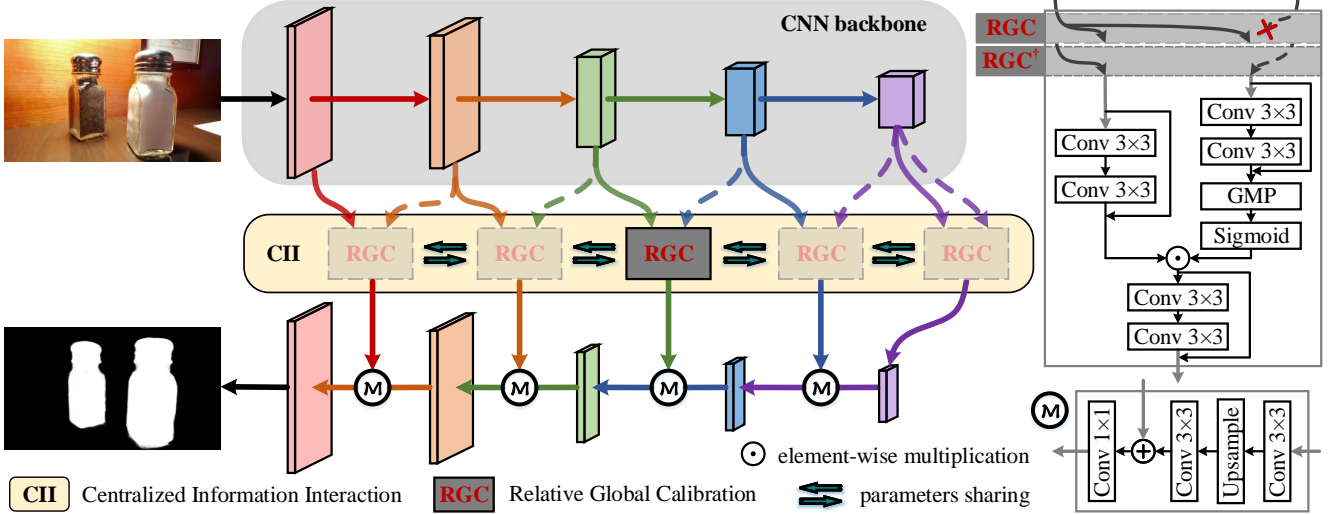


Figure 3. The overall pipeline of our proposed approach. Note that the dashed arrows only active in RGC^\dagger , as shown in the top-right corner.

information of multiple scales with pooling operations. Recently, Auto-Deeplab [28] proved that optimal multi-scale modules could be automatically obtained with neural architecture search. CBAM [57] proposed a sequence of channel attention and spatial attention to augment the input features. OCNet [66] adopted self-attention mechanism to augment ASPP with stronger context extraction capability. DANet [10] utilized a parallelism of position attention and channel attention to model long-range dependencies. CC-Net [17] developed a criss-cross attention module to capture the global context in both horizontal and vertical directions.

Different from the above-mentioned modules that use single-scale input, our proposed RGC module takes multi-scale inputs simultaneously. Also, our proposed CII aims to augment the information interaction among the connections between the bottom-up and top-down pathways of the U-shape structure rather than the pathways themselves.

3. Method

In this section, we first introduce the overall pipeline of the proposed approach. We then detailedly describe the two main components of the proposed approach, including an information interaction strategy and a feature calibration module.

3.1. Overall Pipeline

The proposed approach is based on the widely used U-shape structure, which consists of a bottom-up pathway for multi-level feature extraction and a top-down pathway to combine them. As illustrated in Fig. 3, the multi-scale features extracted from the bottom-up pathway are parallelly forwarded through the information interactors (solid gray rectangles) stage-wisely. We share the parameters of these information interactors to achieve efficient cross-scale

information interaction by learning more powerful filters. Then the interacted features are progressively used to build the top-down pathway from high- to low-levels. We call the above information interaction strategy that encodes the multi-scale information into the shared filters as centralized information interaction (CII). Considering that the input features of CII are now of multiple scales, we further introduce a relative global calibration (RGC) module to cooperate with it. RGC achieves a balance between essential global semantics and local textures by adaptively exploiting the relative global information concerning each different input scale. In the following subsections, we describe the above-mentioned strategy and module in detail.

3.2. Centralized Information Interaction

One typical design in the classic U-shape structure is the short connections between the stages of the same spatial scales from the bottom-up pathway to the top-down pathway. This design provides a simple and efficient way to combine the extracted multi-level feature maps. Taking the ResNet-18 [13] version of the classic U-shape structure for example, the feature maps outputted by conv1, res1, res2, res3, res4 which are denoted by $\mathbb{B} = \{B_i\}$ ($1 \leq i \leq M$ and $M = 5$) are usually used to build the output feature pyramid of the bottom-up pathway. In the top-down pathway, the most high-level feature map is progressively up-sampled and then aggregated with the feature map of the corresponding down-sampling rate. As can be noticed, feature map B_i can not get information from feature maps belonging to higher stages B_j ($1 \leq i < j \leq M$) until it is aggregated with B_{i+1} in the top-down pathway. Suppose we treat the connections between the bottom-up and top-down pathways as an independent part. In that case, the information flows of different scales inside this part are independent and unknown to each other.

The insightful point that lower-level features contain more local textures and patterns while the higher-level ones indicate the locations of the entire target objects manifests the necessity of augmenting the interaction among them to complement all features with more accurate localization and more precise segmentation capabilities. To this end, we propose to enhance the information interaction among the multi-scale feature maps when they are transmitted from the bottom-up to the top-down pathways.

As shown in the rounded yellow rectangle of Fig. 3, compared to the classic U-shape structure that directly delivers the extracted multi-scale feature maps to the top-down pathway, CII utilizes a series of identical information interactors (solid gray rectangles) to interact the information encoded in them. These information interactors are placed at the center of the classic U-shape structure and the parameters of them are shared. In this way, by being encoded into the shared learnable filters, the multi-scale informations can interact with each other. Note that CII is not a specific module but a strategy. The design of the information interactors in CII is flexible and can be replaced with various successful modules [3, 57, 65, 71] to have inputs and outputs of identical shapes.

When basing on the ResNet-18 backbone, the channel numbers corresponding to \mathbb{B} are set to $\{64, 64, 128, 256, 512\}$, respectively. We apply a 1×1 convolution layer ($f_i^{1 \times 1}$) after each $B_i \in \mathbb{B}$ to map the input channels to the same output channel (*i.e.*, 64). Note that in the following parts of the paper, we omit the batch normalization layer (BN [18]) and non-linear activation layer (ReLU [38]) after each convolution layer for notational convenience. The mapped feature maps are processed by the information interactors to obtain the output feature maps of CII: $\mathbb{C} = \{C_i\}$ ($1 \leq i \leq M$ and $M = 5$), respectively. The overall process of CII can be summarized as:

$$C_i = InI_i(f_i^{1 \times 1}(B_i)), 1 \leq i \leq M, \quad (1)$$

where C_i and B_i are of the same spatial shapes, and InI_i refers to the identical information interactors whose parameters are shared for every i . \mathbb{C} are then used to build the top-down pathway.

Quite different from the previous methods [26, 39] that achieve information interaction by directly fusing the multi-scale features (*e.g.*, concatenation or summation), our CII encodes the information into the shared learnable filters. The information interactors in CII can get optimization signals from both high- and low-level features, resulting in semantically stronger and positionally more precise patterns. One advantage of CII is that the aliasing effect of up-sampling is fundamentally avoided, as the input and output feature maps of each information interactor are of the same spatial sizes, indicating that no spatial interpolation opera-

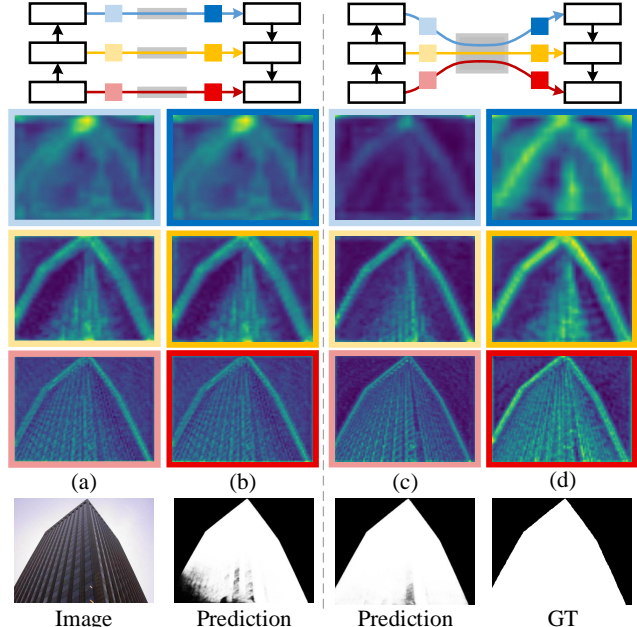


Figure 4. Visualizing feature maps w/o and w/ CII. Every translucent gray rectangle refers to a sequence of two 3×3 convolution layers. As can be seen, CII can interact the complementary information encoded in feature maps of different scales (c,d). For comparison, w/o CII, the feature maps are roughly unchanged (a,b).

tion is required. Also, CII only introduces a small number of additional parameters since we do not need individual modules for each scale of inputs.

To have a straightforward perception, we show some visual comparisons of the intermediate feature maps around CII in Fig. 4. For simplicity and without loss of generality, we use a sequence of two 3×3 convolution layers as the information interactors (parameters are shared) in this section to build CII. If we leave the information interactors independent of each other (parameters not shared), we obtain a simple basic U-shape structure baseline. By comparing the 4th with the 3rd columns of Fig. 4, we can see that after CII, the lower-level features tend to highlight more structural pixels than only the exact edge pixels. The higher-level features, on the contrary, become more detailed around the objects' boundaries. In contrast, without CII, the feature maps after and before the information interactors are roughly the same (the 2nd *v.s.* 1st columns in Fig. 4). This phenomenon verifies the significant effect of our CII on complementing the information across scales.

3.3. Relative Global Calibration

CII introduces a new strategy for efficient cross-scale information interaction against the classic U-shape structure. As aforementioned, when building the information interactors, a simple sequence of two 3×3 convolution layers outperforms its baseline version with a considerable mar-

gin (the 3rd v.s. 2nd rows in Table. 1).

It is well-known in segmentation-like tasks that an effective multi-scale module would always promote the overall performance. For example, the famous PPM [71] comprises four parallel pooling branches with different down-sampling rates to utilize the input feature maps’ multi-scale information. It was first introduced in semantic segmentation and has been successfully adopted in many salient object detection methods [30, 48]. Based on this prior and that PPM is designed to be plug-and-play, we try to use it as the information interactors in CII (InI_i in Equ. 1). However, it turns out that PPM does not work well with CII (the 4th v.s. 1st rows in Table. 2).

PPM was designed to collect information from multiple receptive field sizes when the input is single-scale. When the inputs are of multiple scales (*i.e.*, \mathbb{B}), it results in a rapid growth of receptive fields sizes (*i.e.*, 1×4 v.s. $M \times 4$). However, as pointed out in a lot of previous literature [3, 31, 71], more diversity does not necessarily mean better results, which can even be problematic as too much diversity may distract the following layers.

Considering that the inputs of CII (*i.e.*, \mathbb{B}) naturally have multiple receptive field sizes, it is essential to cut off the redundancy and retain only the necessary diversity. We propose a relative global calibration module that contains two parallel branches responsible for local information retainment and relative global information compaction, as illustrated in the top-right part of Fig. 3. Specifically, in both the two branches of RGC, $B_i \in \mathbb{B}$ is first processed by a sequence of two 3×3 convolution layers (denoted as $f_{L_2}^{3 \times 3}$ and $f_{R_2}^{3 \times 3}$, respectively). The learnable parameters in these layers leave moderate rooms for feature adjustment as the spatial scales of the feature maps in \mathbb{B} differ. Then a global max pooling layer (GMP) is applied after the convolution layers in the right branch to compact the relative global information G_i concerning B_i :

$$G_i = \sigma(GMP((f_{R_2}^{3 \times 3} + 1)(B_i))), 1 \leq i \leq M, \quad (2)$$

where σ refers to the sigmoid function. After that, the compacted global information from the right branch is used to calibrate the retained local feature from the left branch. With another sequence of two 3×3 convolution layers ($f_{F_2}^{3 \times 3}$), we can obtain the output R_i :

$$R_i = (f_{F_2}^{3 \times 3} + 1)(G_i \odot (f_{L_2}^{3 \times 3} + 1)(B_i)), 1 \leq i \leq M. \quad (3)$$

Note that all the learnable parameters in Equ: 2 and 3 are shared for every i .

We will show in Sec. 4 that when cooperating with CII, though with fewer branches, RGC outperforms the previous multi-scale modules. To investigate the potential of RGC, we make a small modification to the inputs of RGC to lead in global information of larger receptive fields without interpolating the inputs spatially. By simply replacing the input

of the right branch with the feature map from its succeeding stage (*i.e.*, B_i to $B_i + 1$), we get RGC[†] which can further improve the performances while introducing no additional parameters and having even less computation complexity. We will provide more quantitative analysis in the experiment section.

4. Experiments

4.1. Experiment Setup

Datasets: For all the experiments, the DUTS-TR [47] dataset is used for training as commonly done. For performance evaluation, five popular datasets: ECSSD [63], PASCAL-S [25], DUT-OMRON [64], HKU-IS [22] and DUTS-TE [47] are used.

Loss Function: We utilize the summation of binary cross entropy (BCE) loss and intersection over union (IoU) loss as our loss function:

$$l = l_{bce} + l_{iou}. \quad (4)$$

BCE loss is broadly used in binary classification and segmentation tasks due to its robustness, which accumulates per-pixel loss in images:

$$l_{bce}(x, y) = -\frac{1}{n} \sum_{k=1}^n [y_k \log(x_k) + (1 - y_k) \log(1 - x_k)], \quad (5)$$

where x and y denote the predicted map and the ground truth respectively, while k is the index of pixels and n is the number of pixels in x . Different from BCE loss that focuses on the pixel-level differences, IoU loss takes into account the similarity of the whole image, which is defined as follows:

$$l_{iou}(x, y) = 1 - \frac{\sum_{k=1}^n (y_k * x_k)}{\sum_{k=1}^n (y_k + x_k - y_k * x_k)}. \quad (6)$$

Evaluation Criteria: We evaluate the performance of our approach and other methods using four widely-used metrics: precision-recall (PR) curves, F-measure score (F_β), S-measure score (S_α) [8], and mean absolute error (MAE). The F-measure(F_β) score is formulated as the weighted harmonic mean of the average precision and average recall:

$$F_\beta = \frac{(1 + \beta^2) \times Precision \times Recall}{\beta^2 \times Precision + Recall}. \quad (7)$$

We set β^2 to 0.3 to weigh precision more than recall as the previous works suggested. The S-measure (S_α) score reflects both the object-aware (S_o) and the region-aware (S_r) structure similarities between the predicted map and the ground truth:

$$S_\alpha = \gamma S_o + (1 - \gamma) S_r, \quad (8)$$

where γ is set as 0.5 by default. The MAE score evaluates

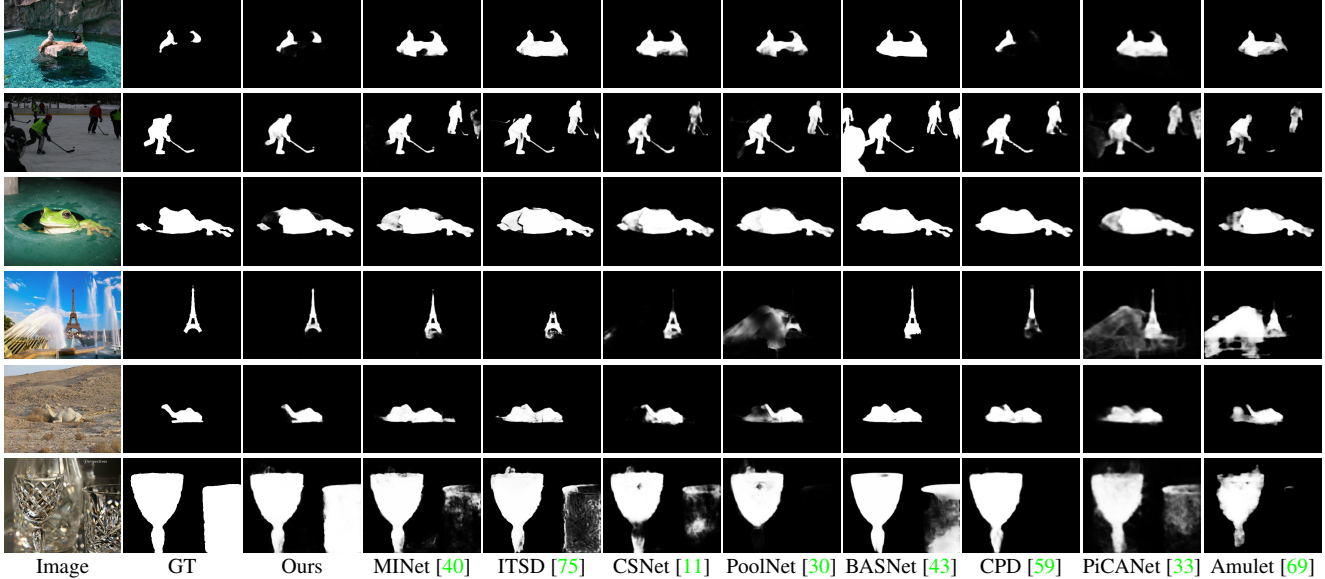


Figure 5. Qualitative comparisons to previous state-of-the-art methods. Compared to other methods, our approach can not only locate the salient objects with cluttered backgrounds but also produce more integral saliency maps.

the average pixel-level relative error between the normalized predicted map P and ground truth G :

$$MAE = \frac{1}{W \times H} \sum_{x=1}^W \sum_{y=1}^H |P(x, y) - G(x, y)|, \quad (9)$$

where W and H denote the width and height of P , respectively.

Implementation Details: We implement our approach using the publicly available PyTorch library¹ and a RTX-2080Ti GPU is used for acceleration. The parameters of our backbone network (*i.e.*, ResNet-18 and ResNet-50 [13]) are initialized with the corresponding models pretrained on the ImageNet dataset [20] and the rest are randomly initialized. For all the experiments, our model is trained for 32 epochs with a batch size of 30. The stochastic gradient descent (SGD) optimizer with a momentum of 0.9 and weight decay of $5e-5$ is used for optimization. The maximum learning rates are set as 0.005 for the backbone and 0.05 for the rest. We apply warm-up and cosine schedule to the learning rates in the first 8 and last 24 epochs, respectively. Random horizontal flipping and random cropping are used for data augmentation. In both training and testing, the input images are resized to 352×352 . By default, our ablation experiments are based on the ResNet-18 [13] backbone unless special explanations. Note that we do not apply any pre- or post-processing techniques.

4.2. Ablation Studies

In this subsection, we first conduct several straightforward experiments to show the effectiveness of the purposed

¹<https://pytorch.org>

CII and RGC from an overall perspective. Then we detailedly investigate the design choices and analyze the configurations of both CII and RGC with more ablation studies.

Effectiveness of CII: To demonstrate the effectiveness of CII against the classic U-shape structure, we compare different settings of the connections between the bottom-up and top-down pathways in Table. 1. Except for the settings of the connections, all other configurations are identical. The 1st row in Table. 1 is the U-shape baseline which connects the bottom-up and top-down pathways with a single 1×1 convolution layer, respectively. As a comparison, the 3rd row applies our proposed CII with a sequence of two 3×3 convolution layers as the information interactor (InI_i in Equ. 1), which is shared across scales. As can be seen, the utilization of CII greatly promotes the overall performances compared to the U-shape baseline.

- **The Influence of Additional Parameters.** To eliminate the influence of introducing more parameters, we replace every 1×1 convolution layer in the model of the 1st row with a sequence of two 3×3 convolution layers (M sequences, $2 \times M$ convolution layers in total), as shown in the 2nd row of Table. 1. With more convolutional layers, the overall performances are slightly improved (the 2nd *v.s.* 1st rows). However, there is still a large margin compared to CII (the 2nd *v.s.* 3rd rows). This phenomenon demonstrates that more parameters do not necessarily mean better performance. A similar conclusion can be drawn by comparing the 4th with the 3rd rows in Table. 1.
- **Visualization of the Features.** The utilization of CII enables the previous independent multi-scale features

Kernel Size	No.	Share	DUT-OMRON [64]			DUTS-TE [47]		
			$F_\beta \uparrow$	MAE \downarrow	$S_\alpha \uparrow$	$F_\beta \uparrow$	MAE \downarrow	$S_\alpha \uparrow$
1×1	$1 \times M$	✗	0.801	0.075	0.816	0.848	0.060	0.851
3×3	$2 \times M$	✗	0.804	0.075	0.818	0.849	0.059	0.852
3×3	2×1	✓	0.810	0.069	0.822	0.869	0.050	0.870
3×3	4×1	✓	0.812	0.066	0.825	0.868	0.049	0.870

Table 1. Ablation analysis of the proposed CII strategy on two popular datasets. M refers to the number of connections between the bottom-up and top-down pathways. The best result in each column is highlighted in **red**.

to interact with each other before being used to build the top-down pathway. We visualize the intermediate features after the bottom-up pathway and before the top-down pathway in Fig. 4. Columns (a,b) are obtained from the model described in the 2nd row of Table. 1, while columns (c,d) are from the 3rd row. As can be seen, with the help of CII, the lower-level features tend to highlight the whole building while the indistinct higher-level features become more confident on the building’s boundaries. On the opposite, without CII, the feature maps are visually identical.

Effectiveness of RGC: To prove the effectiveness of RGC, we conduct a series of ablation experiments comparing different settings of the centralized information interactors (InI_i in Equ: 1). Note that in the following experiments, except for the information interactor itself, all other configurations are identical to the 4th row in Table. 1.

- **RGC v.s. 3×3 Convs.** As can be seen from the 2nd row compared to the 1st row in Tab. 2, with the help of the RGC module, better overall performances are reached. This proves the effectiveness of introducing an extra branch to calibrate the local feature with its relative global information within each specific input scale.
- **RGC v.s. PPM.** To investigate the effectiveness of previous multi-scale modules, we migrate the successful PPM [71] module into CII by directly replacing the RGC module with it. However, as shown in the 4th row in Table. 2, PPM even performs slightly worse than those with only 3×3 convolution layers (the 1st row). These numerical results indicate that the previous successful multi-scale modules may not necessarily succeed in CII.
- **RGC[†] v.s. RGC.** RGC[†] changes the input of its right (relative global) branch to be the feature of the succeeding stage (B_i to B_{i+1}). By comparing the 3rd to 2nd rows in Table. 2, we can see that the performances are further promoted. We also try PPM[†] (the 5th row), which is obtained by changing the inputs of the

Information Interactor	DUT-OMRON [64]			DUTS-TE [47]		
	$F_\beta \uparrow$	MAE \downarrow	$S_\alpha \uparrow$	$F_\beta \uparrow$	MAE \downarrow	$S_\alpha \uparrow$
3×3 Convs	0.812	0.066	0.825	0.868	0.049	0.870
RGC	0.820	0.061	0.826	0.873	0.045	0.870
RGC [†]	0.824	0.058	0.828	0.878	0.042	0.874
PPM [71]	0.810	0.066	0.826	0.868	0.047	0.868
PPM [†]	0.803	0.070	0.821	0.866	0.047	0.869

Table 2. Ablation analysis of the proposed RGC module on two popular datasets. The 1st row uses a sequence of four 3×3 convolution layers as the information interactor (the same as the 4th row in Table. 1). The best result in each column is highlighted in **red**.

branches with spatial interpolation operations in PPM to be the feature of the succeeding stage. However, the results are not satisfactory. These phenomenons show a promising direction of developing new multi-scale modules better cooperating with CII.

4.3. Comparisons to the State-of-the-Arts

In this section, we compare our proposed approach with 15 previous state-of-the-art methods, including DCL [23], DSS [15], Amulet [69], RAS [4], PiCANet [33], AFNet [9], MLMS [58], JDFPR [62], PAGE [53], CPD [59], BASNet [43], PoolNet [30], CSNet [11], ITSD [75], and MINet [40]. For fair comparisons, the saliency maps of other methods are generated by the original codes released by the corresponding authors or directly provided by them. We evaluate all the results with the same evaluation codes.

Quantitative Comparisons Quantitative results are listed in Table. 3. As can be seen, the ResNet-50 version of our proposed approach achieves the best performances on most of the datasets and metrics. We only introduce 0.97M (4.1%) additional parameters compared to the ResNet-50 backbone (23.51M). Especially, the RGC module only occupies 0.22M (0.9%) parameters while the other 0.75M (3.2%) parameters are essential components to construct the top-down pathway. When compared to the previous most efficient method ITSD [75] (based on ResNet-50), our method achieves obvious better results on most of the datasets while requiring 67% less additional parameters (0.97M v.s. 2.96M) and 14% less additional FLOPs (4.74G v.s. 5.53G)

We also show the results of the ResNet-18 version of our approach in Table. 3. Surprisingly, our ResNet-18 version still outperforms most of the previous methods based on the more powerful ResNet-50 network with even fewer parameters and FLOPs. Besides the numerical comparison, we also show the PR curves on three datasets in Fig. 6. It is obvious that the PR curves of our approach (red ones) surpass almost all other methods under most thresholds. This verifies the robustness of our approach.

Method	Params (M)	FLOPs (G)	ECSSD [63]			PASCAL-S [25]			DUT-OMRON [64]			HKU-IS [22]			DUTS-TE [47]		
			$F_\beta \uparrow$	MAE \downarrow	$S_\alpha \uparrow$	$F_\beta \uparrow$	MAE \downarrow	$S_\alpha \uparrow$	$F_\beta \uparrow$	MAE \downarrow	$S_\alpha \uparrow$	$F_\beta \uparrow$	MAE \downarrow	$S_\alpha \uparrow$	$F_\beta \uparrow$	MAE \downarrow	$S_\alpha \uparrow$
DCL ₁₆ [23]	66.25	-	0.898	0.078	0.873	0.805	0.115	0.800	0.733	0.094	0.762	0.893	0.063	0.871	0.786	0.081	0.803
DSS ₁₇ [15]	62.23	52.20	0.908	0.062	0.884	0.821	0.101	0.804	0.760	0.074	0.789	0.900	0.050	0.881	0.813	0.065	0.826
Amulet ₁₇ [69]	33.16	20.70	0.913	0.060	0.881	0.826	0.092	0.816	0.737	0.083	0.784	0.889	0.052	0.866	0.773	0.075	0.800
RAS ₁₈ [4]	20.23	21.24	0.921	0.056	0.893	0.829	0.101	0.799	0.786	0.062	0.814	0.913	0.045	0.887	0.831	0.059	0.839
PiCANet ₁₈ [33]	47.22	54.06	0.935	0.047	0.917	0.864	0.075	0.854	0.820	0.064	0.830	0.920	0.044	0.904	0.863	0.050	0.868
AFNet ₁₉ [9]	25.78	-	0.936	0.042	0.914	0.861	0.070	0.849	0.820	0.057	0.825	0.926	0.036	0.906	0.867	0.045	0.867
MLMS ₁₉ [58]	74.38	58.18	0.930	0.045	0.911	0.853	0.074	0.844	0.793	0.063	0.809	0.922	0.039	0.907	0.854	0.048	0.862
JDFPR ₁₉ [62]	87.61	42.96	0.928	0.049	0.907	0.854	0.082	0.841	0.802	0.057	0.821	-	-	-	0.833	0.058	0.836
PAGE ₁₉ [53]	-	-	0.931	0.042	0.912	0.848	0.076	0.842	0.791	0.062	0.825	0.920	0.036	0.904	0.838	0.051	0.855
CPD ₁₉ [59]	47.85	7.23	0.939	0.037	0.918	0.859	0.071	0.848	0.796	0.056	0.825	0.925	0.034	0.907	0.865	0.043	0.869
BASNet ₁₉ [43]	87.06	97.65	0.942	0.037	0.916	0.857	0.076	0.838	0.811	0.057	0.836	0.930	0.033	0.908	0.860	0.047	0.866
Ours(ResNet-18)	11.89	6.49	0.941	0.039	0.916	0.868	0.068	0.851	0.824	0.058	0.828	0.933	0.032	0.912	0.878	0.042	0.874
PoolNet ₁₉ [30]	68.26	38.19	0.944	0.039	0.921	0.865	0.075	0.850	0.830	0.055	0.836	0.934	0.032	0.917	0.886	0.040	0.883
CSNet ₂₀ [11]	36.37	11.75	0.944	0.038	0.921	0.866	0.073	0.851	0.821	0.055	0.831	0.930	0.033	0.911	0.881	0.040	0.879
ITSD ₂₀ [75]	26.47	9.67	0.947	0.035	0.925	0.871	0.066	0.859	0.823	0.061	0.840	0.933	0.031	0.916	0.883	0.041	0.885
MINet ₂₀ [40]	162.38	42.73	0.947	0.034	0.925	0.874	0.064	0.856	0.826	0.056	0.833	0.936	0.028	0.920	0.888	0.037	0.884
Ours(ResNet-50)	24.48	8.88	0.950	0.034	0.926	0.882	0.062	0.865	0.831	0.054	0.839	0.939	0.029	0.919	0.890	0.036	0.888

Table 3. Quantitative comparisons on five widely used datasets. The best and second-best results in each column are highlighted in **red** and **blue**, respectively. We also show the results of the ResNet-18 version of our approach. Lines in gray or blue mean methods of similar computational complexities (FLOPs), respectively. The FLOPs of all approaches are measured with an input image size of 224×224 .

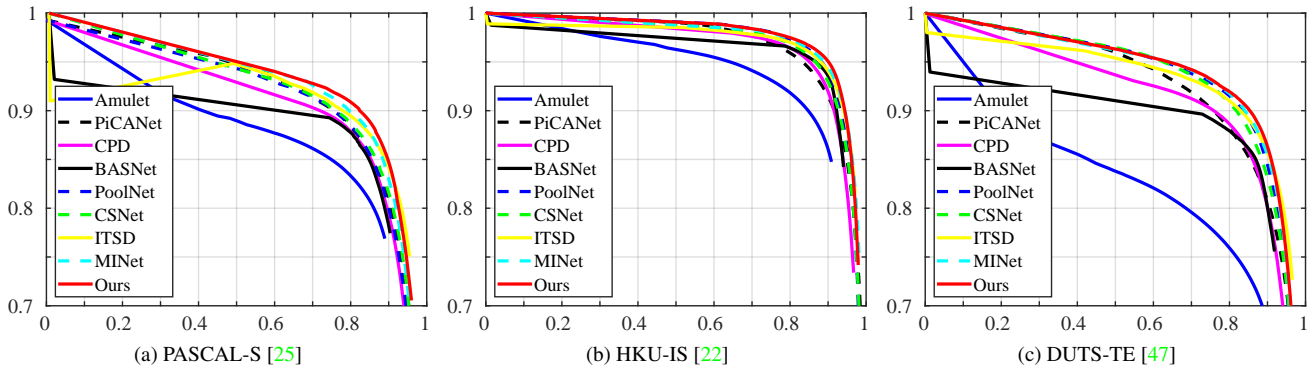


Figure 6. Precision (vertical axis) recall (horizontal axis) curves on three popular salient object detection datasets.

Visual Comparisons: In Fig. 5, we show some representative examples to evaluate our proposed method visually. It can be easily observed that our proposed method can not only accurately highlight the salient objects but also segment them out integrally in almost all circumstances. Different from [29, 53, 60, 72], our approach requires no extra supervision on the edge areas. It demonstrates our method’s effectiveness in augmenting the information interaction among the multi-scale features and generating semantically stronger and positionally more precise features.

5. Conclusions and Future Work

This paper advances the classic U-shape structure by centralizing the previous independent connections between

its bottom-up and top-down pathways to encourage the information interaction among multi-scale features. To show that this centralized information interaction (CII) strategy is feasible, we further propose a relative global calibration (RGC) module to cooperate with it. By combining CII and RGC into the classic U-shape architecture, we show that our proposed approach can surpass all previous state-of-the-art methods on five widely-used salient object detection benchmarks with a handful number of additional parameters and FLOPs. Our proposed strategy and module are independent of the designs of the bottom-up and top-down pathways in the U-shape structures and hence can be flexibly applied to any U-shape based models. Also, the proposed RGC shows a promising direction of developing new multi-scale modules better cooperating with the proposed CII strategy.

References

- [1] Ali Borji, Ming-Ming Cheng, Qibin Hou, Huaizu Jiang, and Jia Li. Salient object detection: A survey. *Computational Visual Media*, 5(2):117–150, 2019. 2
- [2] Ali Borji, Ming-Ming Cheng, Huaizu Jiang, and Jia Li. Salient object detection: A benchmark. *IEEE TIP*, 24(12):5706–5722, 2015. 2
- [3] Liang-Chieh Chen, George Papandreou, Iasonas Kokkinos, Kevin Murphy, and Alan L Yuille. Deeplab: Semantic image segmentation with deep convolutional nets, atrous convolution, and fully connected crfs. *IEEE TPAMI*, 2017. 2, 4, 5
- [4] Shuhan Chen, Xiuli Tan, Ben Wang, Huchuan Lu, Xuelong Hu, and Yun Fu. Reverse attention-based residual network for salient object detection. *IEEE TIP*, 29:3763–3776, 2020. 7, 8
- [5] Ming-Ming Cheng, Niloy J. Mitra, Xiaolei Huang, Philip H. S. Torr, and Shi-Min Hu. Global contrast based salient region detection. *IEEE TPAMI*, 37(3):569–582, 2015. 2
- [6] Ming-Ming Cheng, Fang-Lue Zhang, Niloy J Mitra, Xiaolei Huang, and Shi-Min Hu. Reffinder: finding approximately repeated scene elements for image editing. *ACM TOG*, 29(4):83, 2010. 1
- [7] Celine Craye, David Filliat, and Jean-François Goudou. Environment exploration for object-based visual saliency learning. In *ICRA*, pages 2303–2309, 2016. 1
- [8] Deng-Ping Fan, Ming-Ming Cheng, Yun Liu, Tao Li, and Ali Borji. Structure-measure: A New Way to Evaluate Foreground Maps. In *ICCV*, pages 4548–4557, 2017. 5
- [9] Mengyang Feng, Huchuan Lu, and Errui Ding. Attentive feedback network for boundary-aware salient object detection. In *CVPR*, 2019. 2, 7, 8
- [10] Jun Fu, Jing Liu, Haijie Tian, Yong Li, Yongjun Bao, Zhiwei Fang, and Hanqing Lu. Dual attention network for scene segmentation. In *CVPR*, pages 3146–3154, 2019. 3
- [11] Shang-Hua Gao, Yong-Qiang Tan, Ming-Ming Cheng, Chengze Lu, Yunpeng Chen, and Shuicheng Yan. Highly efficient salient object detection with 100k parameters. In *ECCV*, 2020. 6, 7, 8
- [12] Golnaz Ghiasi, Tsung-Yi Lin, and Quoc V Le. Nas-fpn: Learning scalable feature pyramid architecture for object detection. In *CVPR*, pages 7036–7045, 2019. 2
- [13] Kaiming He, Xiangyu Zhang, Shaoqing Ren, and Jian Sun. Deep residual learning for image recognition. In *CVPR*, 2016. 3, 6
- [14] Seunghoon Hong, Tackgeun You, Suha Kwak, and Bohyung Han. Online tracking by learning discriminative saliency map with convolutional neural network. In *ICML*, pages 597–606, 2015. 1
- [15] Qibin Hou, Ming-Ming Cheng, Xiaowei Hu, Ali Borji, Zhuowen Tu, and Philip Torr. Deeply supervised salient object detection with short connections. *IEEE TPAMI*, 41(4):815–828, 2019. 2, 7, 8
- [16] Qibin Hou, Peng-Tao Jiang, Yunchao Wei, and Ming-Ming Cheng. Self-erasing network for integral object attention. In *NeurIPS*, 2018. 1
- [17] Zilong Huang ; Xinggang Wang ; Yunchao Wei ; Lichao Huang ; Humphrey Shi ; Wenyu Liu ; Thomas S. Huang. Ccnet: Criss-cross attention for semantic segmentation. *IEEE TPAMI*, pages 1–1, 2020. 3
- [18] Sergey Ioffe and Christian Szegedy. Batch normalization: Accelerating deep network training by reducing internal covariate shift. In *ICML*, 2015. 4
- [19] Huaizu Jiang, Jingdong Wang, Zejian Yuan, Yang Wu, Nanning Zheng, and Shipeng Li. Salient object detection: A discriminative regional feature integration approach. In *CVPR*, pages 2083–2090, 2013. 2
- [20] Alex Krizhevsky, Ilya Sutskever, and Geoffrey E Hinton. Imagenet classification with deep convolutional neural networks. In *NeurIPS*, 2012. 6
- [21] Guanbin Li, Yuan Xie, Liang Lin, and Yizhou Yu. Instance-level salient object segmentation. In *CVPR*, 2017. 2
- [22] Guanbin Li and Yizhou Yu. Visual saliency based on multiscale deep features. In *CVPR*, pages 5455–5463, 2015. 5, 8
- [23] Guanbin Li and Yizhou Yu. Deep contrast learning for salient object detection. In *CVPR*, 2016. 7, 8
- [24] Xiaohui Li, Huchuan Lu, Lihe Zhang, Xiang Ruan, and Ming-Hsuan Yang. Saliency detection via dense and sparse reconstruction. In *ICCV*, pages 2976–2983, 2013. 2
- [25] Yin Li, Xiaodi Hou, Christof Koch, James M Rehg, and Alan L Yuille. The secrets of salient object segmentation. In *CVPR*, pages 280–287, 2014. 5, 8
- [26] Zun Li, Congyan Lang, Junhao Liew, Qibin Hou, Yidong Li, and Jiashi Feng. Cross-layer feature pyramid network for salient object detection. *arXiv preprint arXiv:2002.10864*, 2020. 1, 4
- [27] Tsung-Yi Lin, Piotr Dollár, Ross B Girshick, Kaiming He, Bharath Hariharan, and Serge J Belongie. Feature pyramid networks for object detection. In *CVPR*, 2017. 1, 2
- [28] Chenxi Liu, Liang-Chieh Chen, Florian Schroff, Hartwig Adam, Wei Hua, Alan L Yuille, and Li Fei-Fei. Auto-deeplab: Hierarchical neural architecture search for semantic image segmentation. In *CVPR*, pages 82–92, 2019. 3
- [29] Jiang-Jiang Liu, Qibin Hou, and Ming-Ming Cheng. Dynamic feature integration for simultaneous detection of salient object, edge and skeleton. *IEEE TIP*, 29:8652–8667, 2020. 8
- [30] Jiang-Jiang Liu, Qibin Hou, Ming-Ming Cheng, Jiashi Feng, and Jianmin Jiang. A simple pooling-based design for real-time salient object detection. In *CVPR*, 2019. 2, 5, 6, 7, 8
- [31] Jiang-Jiang Liu, Qibin Hou, Ming-Ming Cheng, Changhu Wang, and Jiashi Feng. Improving convolutional networks with self-calibrated convolutions. In *CVPR*, 2020. 5
- [32] Nian Liu and Junwei Han. Dhsnet: Deep hierarchical saliency network for salient object detection. In *CVPR*, 2016. 2
- [33] Nian Liu, Junwei Han, and Ming-Hsuan Yang. Picanet: Learning pixel-wise contextual attention for saliency detection. In *CVPR*, pages 3089–3098, 2018. 2, 6, 7, 8
- [34] Songtao Liu, Di Huang, and Yunhong Wang. Learning spatial fusion for single-shot object detection. *arXiv preprint arXiv:1911.09516*, 2019. 2

- [35] Shu Liu, Lu Qi, Haifang Qin, Jianping Shi, and Jiaya Jia. Path aggregation network for instance segmentation. In *CVPR*, pages 8759–8768, 2018. 2
- [36] Jonathan Long, Evan Shelhamer, and Trevor Darrell. Fully convolutional networks for semantic segmentation. In *CVPR*, pages 3431–3440, 2015. 2
- [37] Zhiming Luo, Akshaya Kumar Mishra, Andrew Achkar, Justin A Eichel, Shaozi Li, and Pierre-Marc Jodoin. Non-local deep features for salient object detection. In *CVPR*, 2017. 2
- [38] Vinod Nair and Geoffrey E Hinton. Rectified linear units improve restricted boltzmann machines. In *ICML*, 2010. 4
- [39] Jiangmiao Pang, Kai Chen, Jianping Shi, Huajun Feng, Wanli Ouyang, and Dahua Lin. Libra r-cnn: Towards balanced learning for object detection. In *CVPR*, pages 821–830, 2019. 1, 4
- [40] Youwei Pang, Xiaoqi Zhao, Lihe Zhang, and Huchuan Lu. Multi-scale interactive network for salient object detection. In *CVPR*, pages 9413–9422, 2020. 2, 6, 7, 8
- [41] Federico Perazzi, Philipp Krähenbühl, Yael Pritch, and Alexander Hornung. Saliency filters: Contrast based filtering for salient region detection. In *CVPR*, pages 733–740, 2012. 2
- [42] Siyuan Qiao, Liang-Chieh Chen, and Alan Yuille. Detectors: Detecting objects with recursive feature pyramid and switchable atrous convolution. *arXiv preprint arXiv:2006.02334*, 2020. 2
- [43] Xuebin Qin, Zichen Zhang, Chenyang Huang, Chao Gao, Masood Dehghan, and Martin Jagersand. Basnet: Boundary-aware salient object detection. In *CVPR*, 2019. 2, 6, 7, 8
- [44] Olaf Ronneberger, Philipp Fischer, and Thomas Brox. U-net: Convolutional networks for biomedical image segmentation. In *MICCAI*, pages 234–241, 2015. 1, 2
- [45] Jinming Su, Jia Li, Yu Zhang, Changqun Xia, and Yonghong Tian. Selectivity or invariance: Boundary-aware salient object detection. In *ICCV*, pages 3799–3808, 2019. 2
- [46] Mingxing Tan, Ruoming Pang, and Quoc V Le. Efficientdet: Scalable and efficient object detection. In *CVPR*, pages 10781–10790, 2020. 2
- [47] Lijun Wang, Huchuan Lu, Yifan Wang, Mengyang Feng, Dong Wang, Baocai Yin, and Xiang Ruan. Learning to detect salient objects with image-level supervision. In *CVPR*, pages 136–145, 2017. 5, 7, 8
- [48] Tiantian Wang, Ali Borji, Lihe Zhang, Pingping Zhang, and Huchuan Lu. A stagewise refinement model for detecting salient objects in images. In *ICCV*, pages 4019–4028, 2017. 2, 5
- [49] Tiantian Wang, Lihe Zhang, Shuo Wang, Huchuan Lu, Gang Yang, Xiang Ruan, and Ali Borji. Detect globally, refine locally: A novel approach to saliency detection. In *CVPR*, pages 3127–3135, 2018. 2
- [50] Wenguan Wang, Qiuxia Lai, Huazhu Fu, Jianbing Shen, and Haibin Ling. Salient object detection in the deep learning era: An in-depth survey. *arXiv preprint arXiv:1904.09146*, 2019. 2
- [51] Wenguan Wang, Jianbing Shen, Ming-Ming Cheng, and Ling Shao. An iterative and cooperative top-down and bottom-up inference network for salient object detection. In *CVPR*, 2019. 2
- [52] Wenguan Wang, Jianbing Shen, Jianwen Xie, Ming-Ming Cheng, Haibin Ling, and Ali Borji. Revisiting video saliency prediction in the deep learning era. *IEEE TPAMI*, 2019. 2
- [53] Wenguan Wang, Shuyang Zhao, Jianbing Shen, Steven C. H. Hoi, and Ali Borji. Salient object detection with pyramid attention and salient edges. In *CVPR*, 2019. 2, 7, 8
- [54] Jun Wei, Shuhui Wang, and Qingming Huang. F3net: Fusion, feedback and focus for salient object detection. In *AAAI*, 2020. 2
- [55] Jun Wei, Shuhui Wang, Zhe Wu, Chi Su, Qingming Huang, and Qi Tian. Label decoupling framework for salient object detection. In *CVPR*, pages 13025–13034, 2020. 2
- [56] Yunchao Wei, Xiaodan Liang, Yunpeng Chen, Xiaohui Shen, Ming-Ming Cheng, Jiashi Feng, Yao Zhao, and Shuicheng Yan. Stc: A simple to complex framework for weakly-supervised semantic segmentation. *IEEE TPAMI*, 2016. 1
- [57] Sanghyun Woo, Jongchan Park, Joon-Young Lee, and In So Kweon. Cbam: Convolutional block attention module. In *ECCV*, pages 3–19, 2018. 3, 4
- [58] Runmin Wu, Mengyang Feng, Wenlong Guan, Dong Wang, Huchuan Lu, and Errui Ding. A mutual learning method for salient object detection with intertwined multi-supervision. In *CVPR*, 2019. 7, 8
- [59] Zhe Wu, Li Su, and Qingming Huang. Cascaded partial decoder for fast and accurate salient object detection. In *CVPR*, 2019. 2, 6, 7, 8
- [60] Zhe Wu, Li Su, and Qingming Huang. Stacked cross refinement network for edge-aware salient object detection. In *ICCV*, 2019. 8
- [61] Hang Xu, Lewei Yao, Wei Zhang, Xiaodan Liang, and Zhenguo Li. Auto-fpn: Automatic network architecture adaptation for object detection beyond classification. In *ICCV*, pages 6649–6658, 2019. 2
- [62] Yingyue Xu, Dan Xu, Xiaopeng Hong, Wanli Ouyang, Ronrong Ji, Min Xu, and Guoying Zhao. Structured modeling of joint deep feature and prediction refinement for salient object detection. In *ICCV*, 2019. 7, 8
- [63] Qiong Yan, Li Xu, Jianping Shi, and Jiaya Jia. Hierarchical saliency detection. In *CVPR*, pages 1155–1162, 2013. 5, 8
- [64] Chuan Yang, Lihe Zhang, Huchuan Lu, Xiang Ruan, and Ming-Hsuan Yang. Saliency detection via graph-based manifold ranking. In *CVPR*, pages 3166–3173, 2013. 5, 7, 8
- [65] Maoke Yang, Kun Yu, Chi Zhang, Zhiwei Li, and Kuiyuan Yang. Denseaspp for semantic segmentation in street scenes. In *CVPR*, pages 3684–3692, 2018. 2, 4
- [66] Yuhui Yuan and Jingdong Wang. Ocnet: Object context network for scene parsing. *arXiv preprint arXiv:1809.00916*, 2018. 3
- [67] Yi Zeng, Pingping Zhang, Jianming Zhang, Zhe Lin, and Huchuan Lu. Towards high-resolution salient object detection. In *ICCV*, pages 7234–7243, 2019. 2
- [68] Lu Zhang, Ju Dai, Huchuan Lu, You He, and Gang Wang. A bi-directional message passing model for salient object detection. In *CVPR*, pages 1741–1750, 2018. 2

- [69] Pingping Zhang, Dong Wang, Huchuan Lu, Hongyu Wang, and Xiang Ruan. Amulet: Aggregating multi-level convolutional features for salient object detection. In *ICCV*, 2017. [2](#), [6](#), [7](#), [8](#)
- [70] Xiaoning Zhang, Tiantian Wang, Jinqing Qi, Huchuan Lu, and Gang Wang. Progressive attention guided recurrent network for salient object detection. In *CVPR*, pages 714–722, 2018. [2](#)
- [71] Hengshuang Zhao, Jianping Shi, Xiaojuan Qi, Xiaogang Wang, and Jiaya Jia. Pyramid scene parsing network. In *CVPR*, 2017. [2](#), [4](#), [5](#), [7](#)
- [72] Jia-Xing Zhao, Jiang-Jiang Liu, Deng-Ping Fan, Yang Cao, Jufeng Yang, and Ming-Ming Cheng. Egnnet:edge guidance network for salient object detection. In *ICCV*, 2019. [2](#), [8](#)
- [73] Ting Zhao and Xiangqian Wu. Pyramid feature attention network for saliency detection. In *CVPR*, 2019. [2](#)
- [74] Xiaoqi Zhao, Youwei Pang, Lihe Zhang, Huchuan Lu, and Lei Zhang. Suppress and balance: A simple gated network for salient object detection. In *ECCV*, 2020. [2](#)
- [75] Huajun Zhou, Xiaohua Xie, Jian-Huang Lai, Zixuan Chen, and Lingxiao Yang. Interactive two-stream decoder for accurate and fast saliency detection. In *CVPR*, pages 9141–9150, 2020. [2](#), [6](#), [7](#), [8](#)
- [76] Barret Zoph and Quoc V Le. Neural architecture search with reinforcement learning. In *ICLR*, 2017. [2](#)